

# 000 001 002 003 004 005 006 007 STAMP: SEQUENCE TRANSFORMATION AND 008 MIXED PRECISION FOR LOW-PRECISION ACTIVATION 009 QUANTIZATION 010 011 012

013 **Anonymous authors**  
014  
015  
016  
017  
018  
019  
020  
021  
022  
023  
024  
025  
026  
027

028 Paper under double-blind review  
029  
030  
031  
032  
033  
034  
035  
036  
037  
038  
039

## ABSTRACT

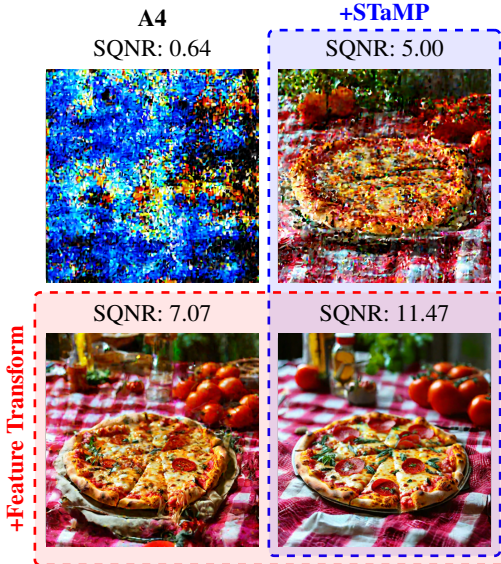
040 Quantization is the key method for reducing inference latency, power and mem-  
041 ory footprint of generative AI models. However, accuracy often degrades sharply  
042 when activations are quantized below eight bits. Recent work suggests that invert-  
043 ible linear transformations (e.g. rotations) can aid quantization, by reparameteriz-  
044 ing feature channels and weights. In this paper, we propose *Sequence Transfor-  
045 mation and Mixed Precision* (STaMP) quantization, a novel strategy that applies  
046 linear transformations along the *sequence* dimension to exploit the strong local  
047 correlation in language and visual data. By keeping a small number of tokens  
048 in each intermediate activation at higher precision, we can maintain model accu-  
049 racy at lower (average) activations bit-widths. We evaluate STaMP on recent  
050 LVM and LLM architectures, demonstrating that it significantly improves low bit  
051 width activation quantization and complements established activation and weight  
052 quantization methods including recent feature transformations.  
053

## 1 INTRODUCTION

054 Modern generative models, such as large lan-  
055 guage models (LLMs) and large vision models  
056 (LVMs), achieve state-of-the-art performance  
057 in text and image generation but at the cost  
058 of massive computational and memory require-  
059 ments. As the demand for scalable and efficient  
060 deployment of these models grows, both in the  
061 cloud and on edge devices where computational  
062 resources are scarce, achieving inference effi-  
063 ciency has become a critical area of research.

064 Post-Training Quantization (PTQ) of weights  
065 and activations is fundamental to enhancing  
066 inference efficiency, especially for demand-  
067 ing operations such as large matrix multiplica-  
068 tions in linear layers, which dominate power  
069 consumption. However, PTQ faces substan-  
070 tial challenges when pushing the quantization  
071 bitwidth down to 4-bits, often due to the pres-  
072 ence of outliers in weights and activations.

073 To mitigate outliers, prior work applies *function-preserving transformations* (van Breugel et al.,  
074 2025) to weights and activations. For example, Xiao et al. (2023) scales down outlier activations and  
075 compensates by scaling up subsequent weights, preserving the model output. Similarly, Hadamard-  
076 based feature mixing (Ashkboos et al., 2024; Liu et al., 2024; Ma et al., 2024; Zhao et al., 2025)  
077 reduces activation variance and spreads outliers across dimensions.



078 Figure 1: STaMP and feature transformations applied to PixArt- $\Sigma$  with 4-bit activations. The benefit of STaMP is orthogonal to (Hadamard) feature transformation, drastically reducing artifacts.

054 However, these methods operate primarily along the feature dimension and ignore correlations  
 055 across the sequence dimension. Drawing inspiration from traditional media compression methods,  
 056 in this paper we propose *Sequence Transformation and Mixed Precision* (STaMP) quantization, a  
 057 complementary approach that leverages sequence structure to improve activation quantization.  
 058

059 Our main contributions are summarized below:

- 060 • We introduce a new class of activation transformations operating along the sequence di-  
 061 mension, complementary to existing feature transformations (Figure 1).
- 062 • We characterize the quantization error for sequence transforms and design a novel mixed-  
 063 precision quantization scheme to exploit local activation correlation.
- 064 • We demonstrate that STaMP consistently improves the model accuracy when combined  
 065 with feature transformations and weight quantization on both LLM and LVM.

## 067 2 BACKGROUND

### 070 2.1 ACTIVATION QUANTIZATION

072 Consider  $\mathbf{X} \in \mathbb{R}^{s \times d}$  as an activation matrix of shape *sequence length*  $s \times$  *feature size*  $d$  (batch  
 073 size is omitted for the sake of clarity). Integer quantization refers to the operation of converting  
 074 the activations to integer values with lower bit width. The activation quantization operation  $\mathbf{Q} : \mathbb{R}^{s \times d} \rightarrow \mathbb{N}^{s \times d}$  is defined as:

$$076 \quad x_{ij}^{\text{int}} \stackrel{\text{def}}{=} \mathbf{Q}(\mathbf{X})_{ij} = \text{clamp}\left(\left\lfloor \frac{x_{ij}}{s_{ij}} \right\rfloor + z_{ij}, 0, 2^{b_{ij}} - 1\right), \quad (1)$$

079 in which  $z_{ij}$  and  $s_{ij}$  can be interpreted as an offset and scaling parameter, while  $b_{ij}$  refers to the  
 080 number of bits used to quantize the entry  $x_{ij}$ . In order to make quantization efficient, offsets, scales  
 081 and bit widths are shared across all feature channels:  $s_{ij} = s_i$ ,  $z_{ij} = z_i$ , and  $b_{ij} = b_i$ .

082 The de-quantization function  $\mathbf{Q}^{-1} : \mathbb{N}^{s \times d} \rightarrow \mathbb{R}^{s \times d}$  maps the integer-quantized activation into the  
 083 original domain:  $\mathbf{Q}^{-1}(\mathbf{X}^{\text{int}})_{ij} = (x_{ij}^{\text{int}} - z_{ij})s_{ij}$ . We will refer to the combination of the quan-  
 084 tization and de-quantization operation with  $\mathcal{Q}(\mathbf{X}) \stackrel{\text{def}}{=} \mathbf{Q}^{-1}(\mathbf{Q}(\mathbf{X}))$ , omitting the quantization  
 085 parameters for brevity. The expected activation quantization error introduced by the quantization  
 086 and de-quantization operations is commonly defined as:

$$088 \quad \mathcal{L}(\mathbf{X}) \stackrel{\text{def}}{=} \mathbb{E} \left[ \|\mathcal{Q}(\mathbf{X}) - \mathbf{X}\|_2^2 \right] = \sum_{i=1}^s \overbrace{\mathbb{E} \left[ \|\mathcal{Q}(\mathbf{x}_i) - \mathbf{x}_i\|_2^2 \right]}^{\mathcal{L}(\mathbf{x}_i)}, \quad (2)$$

091 in which the expectation is computed with respect to the activation distribution  $p(\mathbf{X})$  and  $\|\cdot\|_2^2$  refers  
 092 to the squared Frobenius norm. Nagel et al. (2021) identified two main causes of quantization error:  
 093 clipping error (due to the clamp operator) and rounding error (introduced by the rounding). As is  
 094 common practice in the literature, we will focus on a setting in which the scale  $s_i$  and offset  $z_i$   
 095 for the  $i$ -th token are set based on the range  $(\mathbf{x}_i) \stackrel{\text{def}}{=} \max_j \mathbf{x}_{ij} - \min_j \mathbf{x}_{ij}$  to prevent any clipping  
 096 error:  $\bar{s}_i \stackrel{\text{def}}{=} \frac{2^{b_i} - 1}{\text{range}(\mathbf{x}_i)}$ ,  $\bar{z}_i \stackrel{\text{def}}{=} -\frac{\min_j \mathbf{x}_{ij}}{\bar{s}_i}$ . In this setting, the quantization error for each token  $\mathbf{x}_i$  is  
 097 determined by its quantization scale  $\bar{s}_i$ :

$$099 \quad \mathcal{L}(\mathbf{x}_i) \leq \frac{d}{4} \mathbb{E} [\bar{s}_i^2] = \frac{d}{4} \frac{\mathbb{E} [\text{range}(\mathbf{x}_i)^2]}{(2^{b_i} - 1)^2}. \quad (3)$$

102 As the activation quantization error increases, so does the deterioration in performance for the model  
 103 outputs since the network output diverge from the original (unquantized) model.

### 104 2.2 FEATURE TRANSFORMATIONS

107 In order to reduce the activation quantization error, recent literature has introduced linear function-  
 108 preserving transformations in the form of (right) invertible matrices  $\mathbf{R}$ , which are applied prior to

108 the quantization operation (van Breugel et al., 2025). Clearly, the additional flexibility introduced  
 109 by **Feature Transformations** can aid in reducing the activation quantization error:  
 110

$$111 \quad \mathcal{L}(\mathbf{X}) \geq \min_{\mathbf{R}} \underbrace{\mathbb{E} \left[ \left\| \mathcal{Q}(\mathbf{X}\mathbf{R}) \mathbf{R}^{-1} - \mathbf{X} \right\|_2^2 \right]}_{\mathcal{L}(\mathbf{X}; \mathbf{R})}. \quad (4)$$

114 In particular, rotation matrices can effectively reduce the activation range, effectively spreading  
 115 outliers across multiple channels and consequently reducing the subsequent quantization error:  
 116

$$117 \quad \sum_{i=1}^s \mathbb{E} \left[ \text{range}(\mathbf{x}_i \mathbf{R})^2 \right] \leq \sum_{i=1}^s \mathbb{E} \left[ \text{range}(\mathbf{x}_i)^2 \right] \implies \mathcal{L}(\mathbf{X}; \mathbf{R}) \leq \mathcal{L}(\mathbf{X}) \quad (5)$$

119 Hadamard matrices have proven very effective in reducing the number of outliers with limited ad-  
 120 dditional overhead: matrix multiplications with Hadamard matrices can be performed efficiently in  
 121  $O(s d \log d)$  thanks to the butterfly algorithm (Fino & Algazi, 1976), and the inverse Hadamard  
 122 matrix can be fused into linear layer weights (Ashkboos et al., 2024).

123 Existing feature transformation techniques reduce activation quantization error by redistributing ac-  
 124 tivation ranges across features. However, they operate exclusively along the feature dimension and  
 125 ignore correlations across the sequence dimension. Visual and textual data exhibit strong local cor-  
 126 relations—neighboring pixels in images and adjacent tokens in text are strongly dependent. This  
 127 suggests that a similar structure could exist in the model intermediate activations and could be lever-  
 128 aged to improve quantization efficiency, which is described in the next section.

### 129 3 METHOD

131 We define a **Sequence Transform** as a linear transformation of  $\mathbf{X}$  across sequence dimension de-  
 132 fined by a (left) invertible matrix  $\mathbf{L}$ . Similarly to feature transformations  $\mathbf{R}$ , sequence transforma-  
 133 tions can reduce the quantization error, and the two can be easily combined to further the error:  
 134

$$135 \quad \mathcal{L}(\mathbf{X}) \geq \min_{\mathbf{L}} \underbrace{\mathbb{E} \left[ \left\| \mathbf{L}^{-1} \mathcal{Q}(\mathbf{L}\mathbf{X}) - \mathbf{X} \right\|_2^2 \right]}_{\mathcal{L}(\mathbf{X}; \mathbf{L})} \geq \min_{\mathbf{L}, \mathbf{R}} \underbrace{\mathbb{E} \left[ \left\| \mathbf{L}^{-1} \mathcal{Q}(\mathbf{L}\mathbf{X}\mathbf{R}) \mathbf{R}^{-1} - \mathbf{X} \right\|_2^2 \right]}_{\mathcal{L}(\mathbf{X}; \mathbf{L}, \mathbf{R})}. \quad (6)$$

138 Sequence transformations are linear, hence they commute with other linear operations. For a linear  
 139 layer:  
 140

$$141 \quad (\mathbf{L}^{-1} \mathcal{Q}(\mathbf{L}\mathbf{X})) \mathbf{W} + \mathbf{1}\beta^T = \mathbf{L}^{-1} (\mathcal{Q}(\mathbf{L}\mathbf{X}) \mathbf{W}) + \mathbf{1}\beta^T = \mathbf{L}^{-1} \left( \mathcal{Q}(\mathbf{L}\mathbf{X}) \mathbf{W} + \underbrace{(\mathbf{L}\mathbf{1})\beta^T}_{\ell} \right), \quad (7)$$

143 in which  $\mathbf{1}$  represents a vector of ones of size  $s$ , indicating that the same bias  $\beta$  is applied to all the  
 144 tokens. This implies that we can invert sequence transformation (i) right before applying the bias  
 145 in a linear layer, or (ii) postpone this operation and use a sequence-transformed bias  $\ell\beta^T$  in which  
 146 the scale  $\ell_i$  may differ across different tokens as a function of  $\mathbf{L}$ . The algorithm for a sequence  
 147 transformed linear layer is reported in Figure 2a.

148 We emphasize that, contrary to feature transformations, sequence transforms do not affect weights,  
 149 and hence they are orthogonal to more advanced weight quantization methods such as vector quan-  
 150 tization, GPTQ (Guo et al., 2024), and SVDQuant (Li et al., 2025).

#### 152 3.1 SEQUENCE TRANSFORM AND MIXED PRECISION (STAMP)

154 To understand how sequence transformations affect quantization error, we first formalize the rela-  
 155 tionship between quantization error and sequence-transformed tokens (proof in Appendix A.1):

156 **Theorem 1.** *The expected quantization error for activations  $\mathbf{X}$  transformed by an orthogonal se-  
 157 quence transformation  $\mathbf{L}$  and quantized using a min-max scale for each token is upper-bounded by  
 158 the weighted sum of the expected norm of the transformed tokens:*

$$159 \quad \mathcal{L}(\mathbf{X}; \mathbf{L}) \leq \frac{d}{2} \sum_{i=1}^s \overbrace{\mathbb{E} \left[ \left\| \mathbf{l}_i^T \mathbf{X} \right\|_2^2 \right]}^{e_i} \frac{1}{(2^{b_i} - 1)^2}. \quad (8)$$

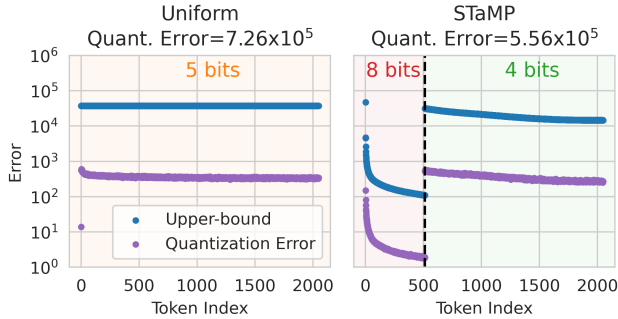
```

162 1: function STaMP LINEAR( $\mathbf{X}$ )
163 2:    $\mathbf{X} \leftarrow \mathbf{L}\mathbf{X}$ 
164 3:   for  $i = 1 \dots s$  do
165 4:      $\mathbf{x}_i \leftarrow \mathbf{Q}(\mathbf{x}_i; b_i)$ 
166 5:   end for
167 6:    $\mathbf{Y} \leftarrow \mathbf{X}\mathbf{W}^T$ 
168 7:    $\mathbf{Y} \leftarrow \mathbf{L}^{-1}\mathbf{Y}$ 
169 8:    $\mathbf{Y} \leftarrow \mathbf{Y} + \beta$ 
170 9:   return  $\mathbf{Y}$ 
171 10: end function

```

172 (a) STaMP Linear Layer Pseudocode

173



(b) Comparison of Upper-Bound and Quantization error

174 **Figure 2: Summary of the STaMP Procedure.** The sequence Transform  $\mathbf{L}$  aims to concentrate  
 175 the energy in the initial tokens, which are quantized at higher precision. This reduces the value of  
 176 the upper-bound in Equation 8 (blue) and, consequently, the overall activation quantization error  
 177 (purple). For a fixed average bit width of 5 bits, combining energy concentration with two precision  
 178 levels (2b, right) achieves lower error than a uniform quantization scheme without sequence trans-  
 179 formations (2b, left). Activations are collected from the input to Layer 20 of LLaMA v3 8B.

180

181

182 Note that sequence transformations  $\mathbf{L}$  do not alter the *total energy*  $E = \sum_{i=1}^s e_i$ , so any improve-  
 183 ment to the bound in Equation 8 must come from redistributing the bit width. This observation  
 184 motivates a mixed precision strategy: instead of keeping energy and bit width uniform, we deliber-  
 185 ately concentrate most of the energy into a few tokens and allocate more bits to them. Because the  
 186 denominator in Equation 8 grows exponentially with  $b_i$ , allocating extra bits to tokens with large  
 187 energy yields a disproportionately large reduction in their contribution to the error. In other words,  
 188 redistributing a bit from a low-energy token to a high-energy token reduces the total error more  
 189 than keeping bit widths and energy uniform. This property is illustrated in Figure 2b and further  
 190 elaborated in Appendix A.3.

191

192 Therefore, to improve activation quantization performance, we propose **Sequence Transform and**  
**Mixed Precision** (STaMP) a simple yet effective strategy that concentrates activation energy into a  
 193 small set of tokens and assigns them higher precision. In the next section, we describe how to design  
 194 a transformation  $\mathbf{L}$  that achieves this efficiently and how to determine the corresponding bit width  
 195 allocation.

196

197

### 3.2 EFFICIENT ENERGY CONCENTRATION

198

199

200 The energy of the  $i$ -th sequence-transformed token  $e_i$  can be also seen as the projection of the  
 201 autocorrelation matrix  $\mathbf{S} = \mathbb{E}[\mathbf{X}\mathbf{X}^T]$  along the direction  $\mathbf{l}_i$ :

202

203

$$e_i = \mathbb{E} \left[ \|\mathbf{l}_i \mathbf{X}\|_2^2 \right] = \mathbf{l}_i^T \mathbf{S} \mathbf{l}_i. \quad (9)$$

204

205

206 he direction that maximizes this energy is the eigenvector  $\mathbf{u}_1$  associated with the largest eigen-  
 207 value  $\lambda_1$  of  $\mathbf{S}$ . Similarly, the second largest energy corresponds to  $\mathbf{u}_2$  and so on. Therefore, given  
 208 the eigendecomposition  $\mathbf{S} = \mathbf{U}\mathbf{\Lambda}\mathbf{U}^T$ , the optimal orthogonal transformation  $\mathbf{L}$  for concentrating  
 209 the token norm is  $\mathbf{U}^T$ . In this case, the energy  $e$  of the transformed tokens  $\mathbf{L}\mathbf{X}$  aligns with the  
 210 squared eigenvalues  $\lambda^2$ . This linear transformation is also known as the **Karhunen-Lo  e Transform**  
 211 (KLT), which requires a representative calibration set to estimate  $\mathbf{U}$ . Despite its optimality,  
 212 KLT has the same computational complexity of a full-rank matrix multiplication, which is imprac-  
 213 tical since each transform needs to be applied twice for each linear layer. Estimating  $\mathbf{S}$  for each  
 214 activation would further adds a costly calibration step.

215

216

217 Fortunately, the autocorrelation matrix of common LVM and LLM activations  $\mathbf{S}$  exhibits a strong  
 218 structure induced by the properties of natural images and text. Figure 3a shows that tokens corre-  
 219 sponding to spatially or sequentially adjacent activations are highly correlated, while distant tokens  
 220 are weakly correlated. As a result  $\mathbf{S}$  is approximately (block) Toeplitz, whose eigenvectors can be

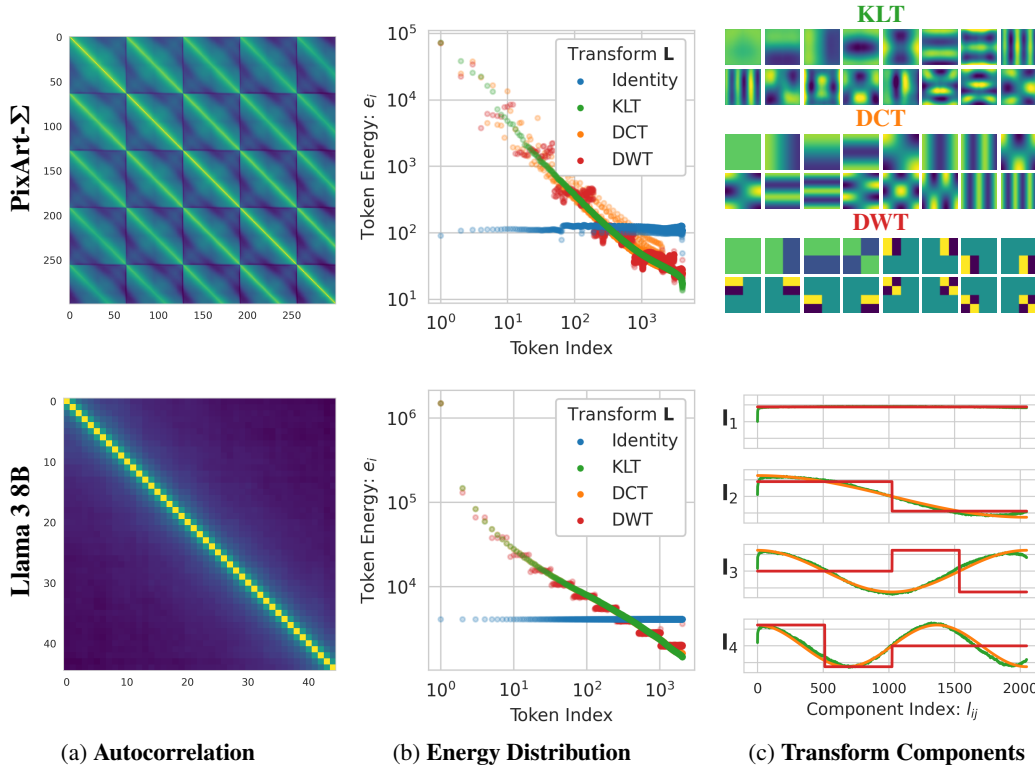


Figure 3: Visualization of (3a) a portion of the autocorrelation matrix, (3b) transformed token energy distribution, and (3c) transformation components for the input to the cross-attention layer 15 of PixArt- $\Sigma$  and the attention layer 20 of LLaMA-v3-8B, computed on COCO and WikiText, respectively. The block structure in the LVM activations arises from flattening 2D data into a 1D sequence. Both matrices exhibit a Toeplitz-like diagonal structure, allowing their **KLT** eigenbases to be efficiently approximated by **DCT** (Figure 3c), which concentrates the token energy close to optimal distribution (Figure 3b). The **DWT** closely approximates the optimal energy with discrete levels.

well-approximated by a Fourier basis<sup>1</sup>. In particular, since the autocorrelation is real and symmetric, we can use a **Discrete Cosine Transform** (DCT) instead of a complex Fourier basis.

The complexity of DCT  $\mathcal{O}(ds \log s)$  is lower than a full matrix multiplication since the transformation requires only  $\log s$  steps of the Fast Fourier Transform algorithm. Further simplification is possible by retaining only the sign of Fourier coefficients, yielding the **Walsh-Hadamard Transform** (WHT), which approximates DCT while enabling more efficient hardware implementations.

Finally, the **Discrete Wavelet Transform** (DWT)<sup>2</sup> further reduces the computational complexity to  $\mathcal{O}(ds)$  while effectively concentrating the energy of the activations at each intermediate step. Each DWT step pushes the energy in the first half (one quarter for 2D signal) of the tokens, requiring  $\log s$  steps to fully concentrate the energy.

Figure 3 compares energy distributions (3b) and basis components (3c) for KLT, DCT, and DWT on intermediate activations of LVM and LLM architectures.

### 3.3 OPTIMAL BIT ALLOCATION

Given a vector of energies  $e$ , the optimal bit distribution  $b$  for a total maximum allocation of  $B$  bits follows the logarithm of the squared root of the token energy:  $b_i^* = \log_2 \sqrt{e_i} - C$ , with  $C = (B - \sum_{i=1}^s \log_2 \sqrt{e_i}) / s$ .  $b^*$  gives us an indication of the optimal bit width for each token, however, in practice we are restricted to integer bit widths  $\lceil b^* \rceil$ . Furthermore, due to practical limitations, it

<sup>1</sup>This follows from Szegő's theorem.

<sup>2</sup>We use the Haar wavelet for its simplicity and minimal padding requirements.

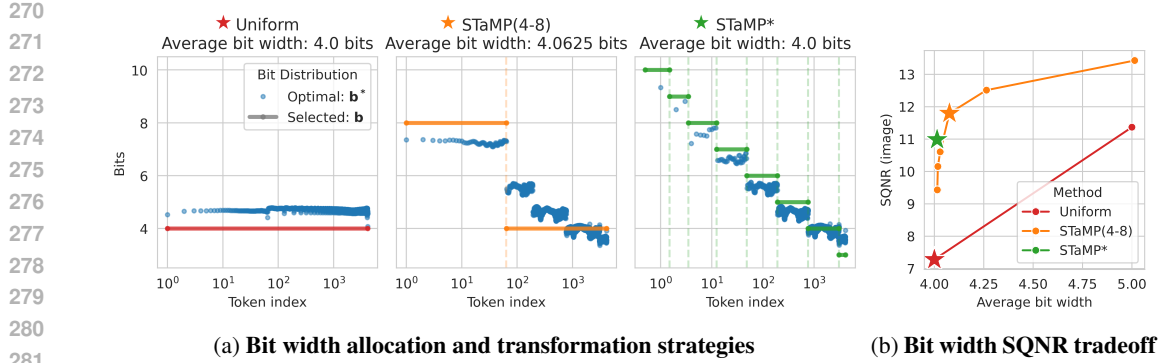


Figure 4: **Comparison of energy and bit width allocation strategies.** Figure 4a compares a uniform allocation without transformation against two STaMP strategies based on the DWT transform. Restricting to only 4- and 8-bits precision (in yellow) introduces minimal overhead while significantly improving output quality. The results in Figure 4b are obtained by varying the number of high-precision tokens and adjusting the uniform quantization bit width for a per token-activation-quantized PixArt- $\Sigma$  model with QuaRot feature transformations.

is beneficial to use only a small number of different bit precisions which are supported on hardware, such as 4 or 8 bits.

For this reason, although the DWT energy concentration is sub-optimal, its property of creating a discrete number of energy levels makes it more suitable to our use case. As illustrated in Figure 4a in yellow, we propose a simple allocation scheme that uses only two bit widths: the first 64 tokens are kept at 8 bits, while the rest uses 4 bits, resulting only in a minor bit width overhead (4.0625 on the PixArt- $\Sigma$ ), while significantly improving the model accuracy (Figure 4b). For this reason, STaMP with DWT and 2 precision level will be our main focus in the experimental section.

## 4 RELATED WORK

Quantization is a fundamental technique for reducing the computational and memory footprint of deep neural networks, enabling efficient inference with minimal accuracy loss. The rapid growth of LLMs and LVMs has intensified interest in post training quantization (PTQ) (Nagel et al., 2021; Gholami et al., 2022), as retraining these models is often impractical. Recent PTQ approaches focus on removing the outliers and reducing the dynamic range of weights and activations, to improve quantization robustness.

SmoothQuant (Xiao et al., 2023) reduces activations outliers by scaling the feature channels, shifting quantization difficulty from activations to weights. *QuaRot* and *FlatQuant* apply invertible feature transforms over weights and activations to spread outliers across channels, employing randomized Hadamard (Ashkboos et al., 2024) or learning lightweight affine transforms (Sun et al., 2025). van Breugel et al. (2025) develop transforms that commute with transformer operations, such that they can be merged into linear weights. Zhao et al. (2025) develops a Static-Dynamic Channel Balancing (SDCB) procedure based on channel scaling and mixing on Diffusion Transformer (DiT) architectures and retaining certain quantization-sensitive layers to higher bitwidth to achieve W8A8. Li et al. (2025) absorbs activation outliers into a high-precision low-rank branch via singular value decomposition, while quantizing the residuals to 4-bit with a per-token/per-group quantization granularity to achieve W4A4 mixed-precision quantization on DiT. Federici et al. (2025) reduces the dynamic range of DiT activations by subtracting the sequence average from each token and applying Hadamard feature rotations, at the cost of processing an extra token.

While these approaches have advanced PTQ for large models, they operate exclusively along the feature dimension and ignore correlations across the sequence dimension. In contrast, STaMP introduces sequence-aware transformations that exploit local token correlations by using a mixed precision allocation strategy under a fixed average budget. Our approach is strongly related to classical media compression techniques that leverage frequency-domain transforms to concentrate energy and

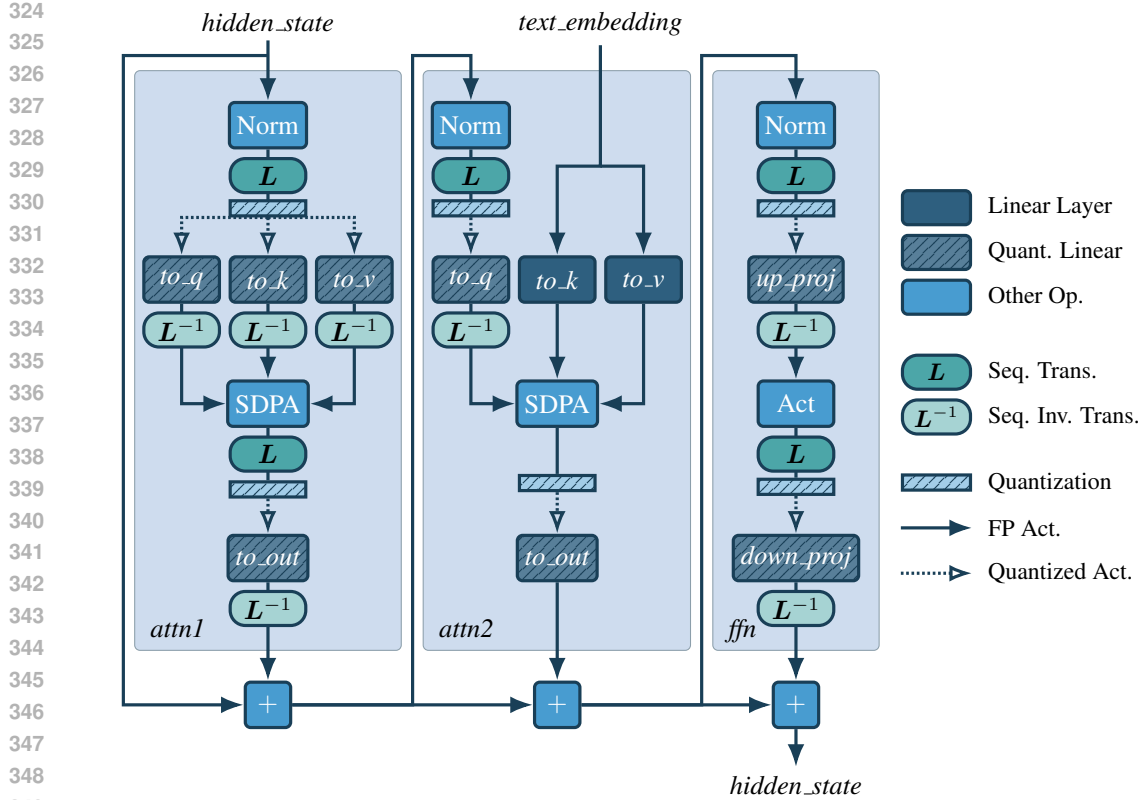


Figure 5: Diagram of a LVM transformer block based on the PixArt- $\Sigma$  architecture. The quantization and sequence transformations operations are indicated explicitly. LLM architectures use the same quantization scheme for the *attn1* and *ffn* blocks. Note that no transform is applied to the *attn2.to\_out* activations since the sequence autocorrelation does not present the block diagonal structure because of its dependency on the pooled textual embedding.

enable adaptive quantization. JPEG (Leger et al., 1991) and JPEG2000 (Christopoulos et al., 2002) rely on the Discrete Cosine Transform and Discrete Wavelet Transform, respectively, to decorrelate spatial data and allocate bits based on perceptual importance. Similar principles underlie modern video coding standards such AVC (Wiegand et al., 2003) and HEVC (Sullivan et al., 2012), as well as audio codecs like MP3 and AAC, which use the Modified Discrete Cosine Transform (Princen et al., 1987). STaMP demonstrates that it is possible to apply similar principles to the activation space of generative models, where local correlation in the sequence dimension allows energy compaction and selective precision allocation, improving quantization efficiency without retraining.

## 5 EXPERIMENTAL RESULTS

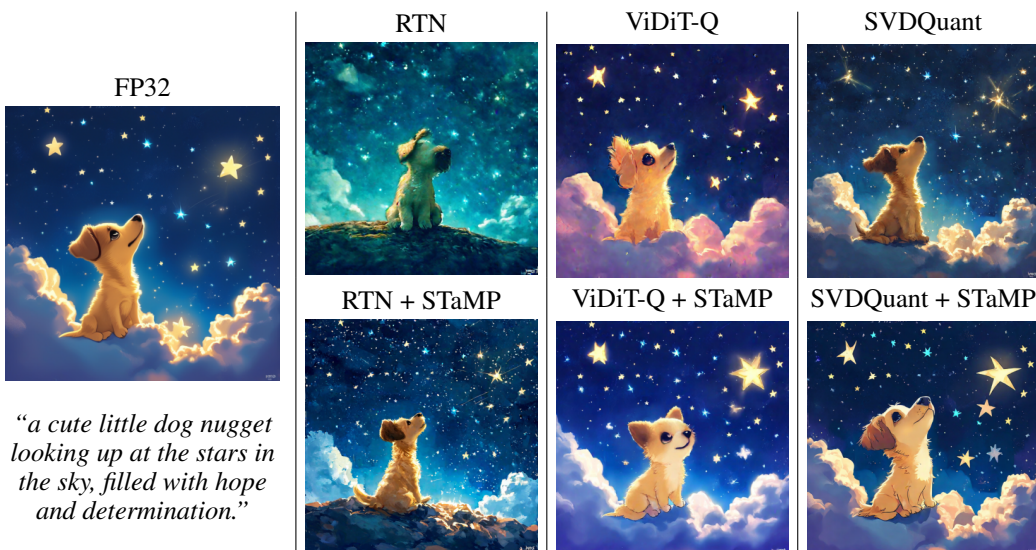
We demonstrate the effectiveness of STaMP on both LVM and LLM models, comparing against uniform activation quantization, and showing its effectiveness in combination with popular feature transformation and weight quantization approaches. Throughout this section, we focus on STaMP with DWT due to its computational efficiency. We refer to Figure 5 for a visualization of how the sequence transformations are applied to the architectures, and to Appendix C for additional results.

### 5.1 VISION LANGUAGE MODELS

**Set-up** Our LVM experiments focus on the DiT architectures of PixArt- $\Sigma$  (Chen et al., 2024b) and SANA (Xie et al., 2025). We quantize activation before each linear layer in transformer blocks using asymmetric quantization with minmax scaling. As common practice, unless otherwise specified, we use a separate scale  $s_i$  for each token and weight output channel. Following common procedure in

378 Table 1: **STaMP consistently improves LVM quantization.** Image SQNR and Image Reward (IR)  
 379 for W4A4 per block quantization with block size 64. For all the STaMP results we keep 64 tokens  
 380 at 8-bits. STaMP consistently improves baselines.

STaMP →	COCO				MJHQ			
	SQNR		IR		SQNR		IR	
	✗	✓	✗	✓	✗	✓	✗	✓
FP	+∞		0.90		+∞		0.96	
PixArt-Σ	RTN	5.88	6.16	0.38	0.80	5.75	6.23	0.38 0.76
	ViDiT-Q	7.82	6.37	0.83	0.84	7.55	8.53	0.76 0.86
	SVDQuant	8.78	9.72	0.90	0.91	8.83	9.75	0.86 0.89
FP	+∞		0.87		+∞		0.97	
SANA	RTN	8.63	9.32	0.89	0.91	8.56	9.40	0.95 0.99
	ViDiT-Q	10.03	10.74	0.89	0.86	10.04	10.69	0.96 0.97
	SVDQuant	9.99	10.69	0.87	0.90	9.88	10.51	0.93 0.98



413 Figure 6: Visualization of PixArt-Σ sample generation for the results reported in Table 1.  
 414  
 415

416 literature, in LVMs we do not quantize activations and weights corresponding to the cross-attention  
 417 key and *value* since their effect accounts for less than 5% of the runtime (Li et al., 2025).

419 We evaluate the fidelity of the quantized LVMs by computing the Signal to Quantized Noise Ratio  
 420  $SQNR(\mathbf{O}_{\text{orig}}, \mathbf{O}_{\text{quant}}) = 10 \log_{10} \left( \|\mathbf{O}_{\text{orig}}\|_2^2 / \|\mathbf{O}_{\text{orig}} - \mathbf{O}_{\text{quant}}\|_2^2 \right)$  both in the diffusion latent space  
 421 and image space. We further compute CLIP Score (Hessel et al., 2021) to assess alignment with  
 422 the textual prompt, CLIP IQA (Wang et al., 2023), and Image Reward (Xu et al., 2023) to evaluate  
 423 the generated image quality. Following standard procedures, we compute the metrics using 1000  
 424 prompts and images from the COCO (Lin et al., 2014) and MJHQ (Li et al., 2024) datasets.

425 We demonstrate the effectiveness STaMP alone and by combining it with other quantization meth-  
 426 ods developed in recent literature. We combine STaMP with feature transform methods such as  
 427 SmoothQuant (Xiao et al., 2023) and QuaRot (Ashkboos et al., 2024), and Static-Dynamic Channel  
 428 Balancing (SDCB) described in ViDiT-Q (Zhao et al., 2025). We further demonstrate the effec-  
 429 tiveness of STaMP with the mixed precision low-rank weight quantization method described in  
 430 SVDQuant (Li et al., 2025). We apply STaMP before each linear layer in the Transformer blocks,  
 431 inverting it right after each linear layer. We use 2-dimensional DWT with 64 8-bit (high precision)  
 tokens unless otherwise specified.

432 Table 2: **STaMP always improves LLM quantization.** Perplexity (PPL) for W4A4KV4 quantization,  
 433 using the same setting as (Ashkboos et al., 2024; Sun et al., 2025). We use 64 8-bit tokens for  
 434 activations and KV-cache for all methods and baselines, even if we do not apply the sequence trans-  
 435 form (effectively W4A4.125KV4.125). The STaMP sequence transform improves all baselines.  
 436

STaMP →	Llama 3 8B		Llama 3.2 1B it		Llama 3.2 3B it		Qwen 2.5 3B it	
	✗	✓	✗	✓	✗	✓	✗	✓
FP	6.14		13.16		11.27		8.56	
RTN	668	95.3	1795	700	483	159	99723	18767
SmoothQuant	531	93.8	883	407	177	88.5	66929	29063
Quarot	9.05	8.66	25.78	23.72	18.43	17.57	94.86	71.13
FlatQuant	6.89	6.77	15.72	15.16	12.71	12.40	9.29	9.19

445  
 446  
 447 **Results** Table 1 reports the results obtained by combining STaMP with recent LVM quantization  
 448 method using the same quantization setting for all the baselines. Both activation and weights are  
 449 quantized at 4 bits with blocks of size 64, following the setup described in (Li et al., 2025). We  
 450 observe that STaMP consistently improves upon all the reported metrics on different models and  
 451 architectures resulting in visually more accurate generations, as shown in Figure 6.  
 452

## 453 5.2 NUMBER OF HIGH PRECISION TOKENS

454  
 455 Figure 4b demonstrates the trade-off between bit width and SQNR observed by changing the number  
 456 of high-precision tokens in STaMP, while fixing the high and low precision bit widths to 8 and  
 457 4 bits respectively. Only activations are quantized to focus the analysis solely on the activation  
 458 quantization error. We observe a sharp increase in SQNR whenever even a few high precision tokens  
 459 are introduced. Even in the 5 bits regime, STaMP achieves better performance uniform quantization.  
 460 Additional comparison with per-block activation quantization can be found in Appendix C.  
 461

## 462 5.3 LARGE LANGUAGE MODELS

463  
 464 **Set-up** We evaluate on language models of different sizes and model classes, including Llama 3  
 465 8B (Grattafiori et al., 2024), Llama 3.2 1B and 3B instruct, and Qwen 2.5 3B instruct (Qwen et al.,  
 466 2025). We take popular *feature* transforms from literature, including SmoothQuant (Xiao et al.,  
 467 2023), QuaRot (Ashkboos et al., 2024), and the state-of-the-art FlatQuant (Sun et al., 2025), and  
 468 evaluate whether STaMP (DWT) brings additional gains to these baselines. We use the exact same  
 469 quantization set-up as used in (Ashkboos et al., 2024; Sun et al., 2025), W4A4KV4 per token activa-  
 470 tion quantization, and like them, evaluate Wikitext-2 (Merity et al., 2017) perplexity at sequence  
 471 length 2048. We use round-to-nearest (RTN) for weight quantization (vs. GPTQ (Frantar et al.,  
 472 2022)), as weight quantization is completely perpendicular to sequence transforms. In this setup,  
 473 we keep the first 64 tokens in 8 bits for all baselines, which means all methods use an effective  
 474 activation/KV bit width of 4.125 bits. Note that, on LLMs, STaMP can be effectively applied only  
 475 for the prompt-processing phase, since during token generation, only one activation is available at  
 476 the time. Despite this limitation, STaMP remains useful for prompt processing, which is typically  
 477 compute-bound (Agrawal et al., 2023; Chen et al., 2024a; Kamath et al., 2025), as reducing the  
 478 activation size lowers total compute and latency. See Appendix B.2 for additional details.  
 479

480  
 481 **Results** We observe (Table 2) that all baselines improve consistently when STaMP is added. This  
 482 is especially apparent for scenarios where baselines are far from FP performance—e.g. for the small  
 483 Llama 3.2 1B and 3B instruct models, which are evidently hard to quantize at 4 bit. This demon-  
 484 strates that STaMP is not a competitor of other quantization techniques (e.g. feature transforms), but  
 485 an additional tool for achieving extremely low bit width quantization—which can be added without  
 any manual tuning or training to existing quantization methods. Appendix C includes additional  
 evaluations on few-shot reasoning tasks, which are consistent with the perplexity measurements.

		SQNR (image)				Image Reward				Wiki-2 Perplexity						
		SDCB	8.09	12.61	12.41	12.50	SDCB	0.83	0.96	0.95	0.97	FlatQuant	6.46	6.34	6.33	6.35
Feature Transform	QuaRot	7.07	11.87	11.88	11.47	QuaRot	0.71	0.94	0.96	0.92	QuaRot	6.86	6.68	6.68	6.69	
	SmoothQuant	5.54	6.40	6.10	6.83	SmoothQuant	-1.87	0.69	0.59	0.52	SmoothQuant	41.06	22.92	23.30	19.25	
	Identity	0.36	5.65	5.11	5.00	Identity	-2.28	0.12	-0.49	-0.99	Identity	111.00	13.53	13.48	22.53	
		Identity	DCT	WHT	DWT		Identity	DCT	WHT	DWT		Identity	DCT	WHT	DWT	
		Sequence Transform				Sequence Transform				Sequence Transform						

(a) A4 PixArt- $\Sigma$  SQNR and Image Reward

(b) A4 Llama v3 8B Perplexity

Figure 7: Effect of combining Feature Transforms (rows) and STaMP (columns) with A4 on the PixArt- $\Sigma$  and LLama v3 8B models.

## 5.4 COMBINING FEATURE AND SEQUENCE TRANSFORMATIONS

In Figure 7 we assess the effectiveness of STaMP for three different sequence transformations in combination with popular feature transforms. Overall, we observe that improvements are largely complementary, especially for LVMs. Furthermore, results show that DCT, WHT and DWT perform similarly to each other, demonstrating that there is little price to pay for switching from the more accurate and computationally expensive DCT to the cheaper approximate DWT.

## 5.5 OVERHEAD ESTIMATES

Table 3 reports that the theoretical compute overhead and latency of CUDA for a latent denoising step with STaMP (DWT) is comparable to Hadamard transforms on the features, accounting for less than 5% of the total runtime. The DWT transform is applied in three levels, consistently with the results reported in Table 1 and Figure 4a, using a specialized CUDA kernel that considers the memory layout of the activation tensors. Appendix B.3 includes further details on the benchmarking procedure. The minimal FLOPS overhead suggests that the latency overhead can be further reduced with better optimized kernels or specialized hardware.

## 6 CONCLUSION

This work explores uncharted territories in the recent advancements of LLM and LVM quantization, applying invertible transformations over the sequence dimension to further reduce quantization error. Drawing inspiration from traditional signal processing, we introduce a novel method that exploits the autocorrelation structure that is naturally present in the intermediate activations of generative models to enable a more efficient mixed-precision activation quantization scheme.

We demonstrate that STaMP complements existing PTQ techniques such as *SmoothQuant* and *QuaRot*, and plays a critical role in advancing low-precision activation quantization, pushing the boundaries of W4A4 quantization for both LLMs and LVMs and offering training-free solution for deploying high-performance models in resource-constrained environments.

Table 3: Overhead in terms of latency on CUDA and extra FLOPS for a single PixArt- $\Sigma$  denoising step. STaMP with DWT has little impact on the latency and number of floating point operations.

Feature	Sequence	Transformation		Overhead [%]	
		FLOPS	CUDA	FLOPS	CUDA
Hadamard	-	0.24	3.0		
-	Hadamard	0.69	56.8		
-	DWT	0.21	4.8		
Hadamard	DWT	0.44	7.8		

540 REFERENCES  
541

542 Amey Agrawal, Ashish Panwar, Jayashree Mohan, Nipun Kwatra, Bhargav S Gulavani, and Ra-  
543 machandran Ramjee. Sarathi: Efficient llm inference by piggybacking decodes with chunked  
544 prefills. *arXiv preprint arXiv:2308.16369*, 2023.

545 Saleh Ashkboos, Amirkeivan Mohtashami, Maximilian L. Croci, Bo Li, Pashmina Cameron, Martin  
546 Jaggi, Dan Alistarh, Torsten Hoefer, and James Hensman. Quarot: Outlier-free 4-bit inference in  
547 rotated llms. In *Advances in Neural Information Processing Systems 38: Annual Conference on  
548 Neural Information Processing Systems 2024, NeurIPS 2024, Vancouver, BC, Canada, December  
549 10 - 15, 2024*, 2024. URL [http://papers.nips.cc/paper\\_files/paper/2024/  
550 hash/b5b939436789f76f08b9d0da5e81af7c-Abstract-Conference.html](http://papers.nips.cc/paper_files/paper/2024/hash/b5b939436789f76f08b9d0da5e81af7c-Abstract-Conference.html).

551 Hao Mark Chen, Fuwen Tan, Alexandros Kouris, Royson Lee, Hongxiang Fan, and Stylianos I  
552 Venieris. Progressive mixed-precision decoding for efficient llm inference. *arXiv preprint  
553 arXiv:2410.13461*, 2024a.

554 Junsong Chen, Chongjian Ge, Enze Xie, Yue Wu, Lewei Yao, Xiaozhe Ren, Zhongdao Wang, Ping  
555 Luo, Huchuan Lu, and Zhenguo Li. Pixart- $\Sigma$ : Weak-to-strong training of diffusion transformer  
556 for 4k text-to-image generation. In *Computer Vision - ECCV 2024 - 18th European Conference,  
557 Milan, Italy, September 29-October 4, 2024, Proceedings, Part XXXII*, volume 15090 of *Lecture  
558 Notes in Computer Science*, pp. 74–91. Springer, 2024b. doi: 10.1007/978-3-031-73411-3\5.  
559 URL [https://doi.org/10.1007/978-3-031-73411-3\\_5](https://doi.org/10.1007/978-3-031-73411-3_5).

560 Charilaos Christopoulos, Athanassios Skodras, and Touradj Ebrahimi. The jpeg2000 still image  
561 coding system: an overview. *IEEE transactions on consumer electronics*, 46(4):1103–1127, 2002.

562 Marco Federici, Riccardo Del Chiaro, Boris van Breugel, Paul Whatmough, and Markus Nagel.  
563 Hadanorm: Diffusion transformer quantization through mean-centered transformations. *arXiv  
564 preprint arXiv:2506.09932*, 2025.

565 Fino and Algazi. Unified matrix treatment of the fast walsh-hadamard transform. *IEEE Transactions  
566 on Computers*, 100(11):1142–1146, 1976.

567 Elias Frantar, Saleh Ashkboos, Torsten Hoefer, and Dan Alistarh. Gptq: Accurate post-training  
568 quantization for generative pre-trained transformers. *arXiv preprint arXiv:2210.17323*, 2022.

569 Leo Gao, Jonathan Tow, Baber Abbasi, Stella Biderman, Sid Black, Anthony DiPofi, Charles Fos-  
570 ter, Laurence Golding, Jeffrey Hsu, Alain Le Noac'h, Haonan Li, Kyle McDonell, Niklas Muen-  
571 nighoff, Chris Ociepa, Jason Phang, Laria Reynolds, Hailey Schoelkopf, Aviya Skowron, Lin-  
572 tang Sutawika, Eric Tang, Anish Thite, Ben Wang, Kevin Wang, and Andy Zou. A framework  
573 for few-shot language model evaluation, 07 2024. URL [https://zenodo.org/records/  
574 12608602](https://zenodo.org/records/12608602).

575 Amir Gholami, Sehoon Kim, Zhen Dong, Zhewei Yao, Michael W Mahoney, and Kurt Keutzer. A  
576 survey of quantization methods for efficient neural network inference. In *Low-power computer  
577 vision*, pp. 291–326. Chapman and Hall/CRC, 2022.

578 Aaron Grattafiori, Abhimanyu Dubey, Abhinav Jauhri, Abhinav Pandey, Abhishek Kadian, Ahmad  
579 Al-Dahle, Aiesha Letman, Akhil Mathur, Alan Schelten, Alex Vaughan, et al. The llama 3 herd  
580 of models. *arXiv preprint arXiv:2407.21783*, 2024.

581 Xiangming Gu, Tianyu Pang, Chao Du, Qian Liu, Fengzhuo Zhang, Cunxiao Du, Ye Wang, and Min  
582 Lin. When Attention Sink Emerges in Language Models: An Empirical View. In *International  
583 Conference on Learning Representations*. arXiv, March 2025. doi: 10.48550/arXiv.2410.10781.  
584 URL <http://arxiv.org/abs/2410.10781>. arXiv:2410.10781 [cs].

585 Yipin Guo, Yilin Lang, and Qinyuan Ren. GPTQT: quantize large language models twice to  
586 push the efficiency. In *IEEE International Conference on Cybernetics and Intelligent Sys-  
587 tems, CIS 2024, and IEEE International Conference on Robotics, Automation and Mechatron-  
588 ics, RAM 2024, Hangzhou, China, August 8-11, 2024*, pp. 368–373. IEEE, 2024. doi: 10.1109/  
589 CIS-RAM61939.2024.10672819. URL [https://doi.org/10.1109/CIS-RAM61939.  
2024.10672819](https://doi.org/10.1109/CIS-RAM61939.2024.10672819).

594 Jack Hessel, Ari Holtzman, Maxwell Forbes, Ronan Le Bras, and Yejin Choi. Clipscore: A  
 595 reference-free evaluation metric for image captioning. In *Proceedings of the 2021 Conference on Empirical Methods in Natural Language Processing, EMNLP 2021, Virtual Event /*  
 596 *Punta Cana, Dominican Republic, 7-11 November, 2021*, pp. 7514–7528. Association for Com-  
 597 *putational Linguistics*, 2021. doi: 10.18653/V1/2021.EMNLP-MAIN.595. URL <https://doi.org/10.18653/v1/2021.emnlp-main.595>.

600 Aditya K Kamath, Ramya Prabhu, Jayashree Mohan, Simon Peter, Ramachandran Ramjee, and  
 601 Ashish Panwar. Pod-attention: Unlocking full prefill-decode overlap for faster llm inference. In  
 602 *Proceedings of the 30th ACM International Conference on Architectural Support for Program-*  
 603 *ming Languages and Operating Systems, Volume 2*, pp. 897–912, 2025.

604 Alain M Leger, Takao Omachi, and Gregory K Wallace. Jpeg still picture compression algorithm.  
 605 *Optical Engineering*, 30(7):947–954, 1991.

606 Daiqing Li, Aleks Kamko, Ehsan Akhgari, Ali Sabet, Linmiao Xu, and Suhail Doshi. Playground  
 607 v2.5: Three insights towards enhancing aesthetic quality in text-to-image generation. *CoRR*,  
 608 abs/2402.17245, 2024. doi: 10.48550/ARXIV.2402.17245. URL <https://doi.org/10.48550/arXiv.2402.17245>.

609 Muyang Li, Yujun Lin, Zhekai Zhang, Tianle Cai, Xiuyu Li, Junxian Guo, Enze Xie, Chenlin Meng,  
 610 Jun-Yan Zhu, and Song Han. Svdquant: Absorbing outliers by low-rank component for 4-bit  
 611 diffusion models. In *The Thirteenth International Conference on Learning Representations, ICLR*  
 612 *2025, Singapore, April 24-28, 2025*. OpenReview.net, 2025. URL <https://openreview.net/forum?id=vWR3KuiQur>.

613 Tsung-Yi Lin, Michael Maire, Serge Belongie, James Hays, Pietro Perona, Deva Ramanan, Piotr  
 614 Dollár, and C. Lawrence Zitnick. Microsoft coco: Common objects in context. In *Computer*  
 615 *Vision – ECCV 2014*, pp. 740–755, Cham, 2014. Springer International Publishing. ISBN 978-3-  
 616 319-10602-1.

617 Zechun Liu, Changsheng Zhao, Igor Fedorov, Bilge Soran, Dhruv Choudhary, Raghuraman Krish-  
 618 namoorthi, Vikas Chandra, Yuandong Tian, and Tijmen Blankevoort. Spinquant: LLM quanti-  
 619 zation with learned rotations. *CoRR*, abs/2405.16406, 2024. doi: 10.48550/ARXIV.2405.16406.  
 620 URL <https://doi.org/10.48550/arXiv.2405.16406>.

621 Yuexiao Ma, Huixia Li, Xiawu Zheng, Feng Ling, Xuefeng Xiao, Rui Wang, Shilei Wen, Fei Chao,  
 622 and Rongrong Ji. Affinequant: Affine transformation quantization for large language models. In  
 623 *The Twelfth International Conference on Learning Representations, ICLR 2024, Vienna, Austria,*  
 624 *May 7-11, 2024*. OpenReview.net, 2024. URL <https://openreview.net/forum?id=of2rhALq81>.

625 Stephen Merity, Caiming Xiong, James Bradbury, and Richard Socher. Pointer sentinel mixture  
 626 models. In *International Conference on Learning Representations*, 2017.

627 Markus Nagel, Marios Fournarakis, Rana Ali Amjad, Yelysei Bondarenko, Mart van Baalen, and  
 628 Tijmen Blankevoort. A white paper on neural network quantization. *CoRR*, abs/2106.08295,  
 629 2021. URL <https://arxiv.org/abs/2106.08295>.

630 J. Princen, A. Johnson, and A. Bradley. Subband/transform coding using filter bank designs based on  
 631 time domain aliasing cancellation. In *ICASSP '87. IEEE International Conference on Acoustics,*  
 632 *Speech, and Signal Processing*, volume 12, pp. 2161–2164, 1987. doi: 10.1109/ICASSP.1987.  
 633 1169405.

634 Qwen, :, An Yang, Baosong Yang, Beichen Zhang, Binyuan Hui, Bo Zheng, Bowen Yu, Chengyuan  
 635 Li, Dayiheng Liu, Fei Huang, Haoran Wei, Huan Lin, Jian Yang, Jianhong Tu, Jianwei Zhang,  
 636 Jianxin Yang, Jiaxi Yang, Jingren Zhou, Junyang Lin, Kai Dang, Keming Lu, Keqin Bao, Kexin  
 637 Yang, Le Yu, Mei Li, Mingfeng Xue, Pei Zhang, Qin Zhu, Rui Men, Runji Lin, Tianhao Li,  
 638 Tianyi Tang, Tingyu Xia, Xingzhang Ren, Xuancheng Ren, Yang Fan, Yang Su, Yichang Zhang,  
 639 Yu Wan, Yuqiong Liu, Zeyu Cui, Zhenru Zhang, and Zihan Qiu. Qwen2.5 technical report, 2025.  
 640 URL <https://arxiv.org/abs/2412.15115>.

648 Gary J. Sullivan, Jens-Rainer Ohm, Woo-Jin Han, and Thomas Wiegand. Overview of the high  
 649 efficiency video coding (hevc) standard. *IEEE Transactions on Circuits and Systems for Video*  
 650 *Technology*, 22(12):1649–1668, 2012. doi: 10.1109/TCSVT.2012.2221191.

651

652 Mingjie Sun, Xinlei Chen, J. Zico Kolter, and Zhuang Liu. Massive Activations in Large Language  
 653 Models. In *First Conference on Language Modeling (COLM)*. arXiv, August 2024. doi: 10.48550/  
 654 arXiv.2402.17762. URL <http://arxiv.org/abs/2402.17762>. arXiv:2402.17762 [cs]  
 655 version: 2.

656 Yuxuan Sun, Ruikang Liu, Haoli Bai, Han Bao, Kang Zhao, Yuening Li, JiaxinHu, Xianzhi Yu,  
 657 Lu Hou, Chun Yuan, Xin Jiang, Wulong Liu, and Jun Yao. Flatquant: Flatness matters for  
 658 LLM quantization. In *Forty-second International Conference on Machine Learning*, 2025. URL  
 659 <https://openreview.net/forum?id=uTz2Utym5n>.

660 Boris van Breugel, Yelysei Bondarenko, Paul Whatmough, and Markus Nagel. Fptquant: Function-  
 661 preserving transforms for llm quantization. *arXiv preprint arXiv:2506.04985*, 2025.

662

663 Jianyi Wang, Kelvin C. K. Chan, and Chen Change Loy. Exploring CLIP for assessing the look and  
 664 feel of images. In *Thirty-Seventh AAAI Conference on Artificial Intelligence, AAAI 2023, Thirty-*  
 665 *Fifth Conference on Innovative Applications of Artificial Intelligence, IAAI 2023, Thirteenth Sym-*  
 666 *posium on Educational Advances in Artificial Intelligence, EAAI 2023, Washington, DC, USA,*  
 667 *February 7-14, 2023*, pp. 2555–2563. AAAI Press, 2023. doi: 10.1609/AAAI.V37I2.25353.  
 668 URL <https://doi.org/10.1609/aaai.v37i2.25353>.

669 T. Wiegand, G.J. Sullivan, G. Bjontegaard, and A. Luthra. Overview of the h.264/avc video coding  
 670 standard. *IEEE Transactions on Circuits and Systems for Video Technology*, 13(7):560–576, 2003.  
 671 doi: 10.1109/TCSVT.2003.815165.

672

673 Guangxuan Xiao, Ji Lin, Mickaël Seznec, Hao Wu, Julien Demouth, and Song Han. Smoothquant:  
 674 Accurate and efficient post-training quantization for large language models. In *International*  
 675 *Conference on Machine Learning, ICML 2023, 23-29 July 2023, Honolulu, Hawaii, USA*, vol-  
 676 *ume 202 of Proceedings of Machine Learning Research*, pp. 38087–38099. PMLR, 2023. URL  
 677 <https://proceedings.mlr.press/v202/xiao23c.html>.

678

679 Guangxuan Xiao, Yuandong Tian, Beidi Chen, Song Han, and Mike Lewis. Efficient Streaming  
 680 Language Models with Attention Sinks. In *International Conference of Learning Representa-*  
 681 *tions*, April 2024. doi: 10.48550/arXiv.2309.17453. URL <http://arxiv.org/abs/2309.17453>. arXiv:2309.17453 [cs].

682

683 Enze Xie, Junsong Chen, Junyu Chen, Han Cai, Haotian Tang, Yujun Lin, Zhekai Zhang, Muyang  
 684 Li, Ligeng Zhu, Yao Lu, and Song Han. SANA: efficient high-resolution text-to-image syn-  
 685 thesis with linear diffusion transformers. In *The Thirteenth International Conference on Learn-*  
 686 *ing Representations, ICLR 2025, Singapore, April 24-28, 2025*. OpenReview.net, 2025. URL  
 687 <https://openreview.net/forum?id=N8Oj1XhtYZ>.

688

689 Jiazheng Xu, Xiao Liu, Yuchen Wu, Yuxuan Tong, Qinkai Li, Ming Ding, Jie Tang, and Yux-  
 690 iao Dong. Imagereward: Learning and evaluating human preferences for text-to-image genera-  
 691 tion. In *Advances in Neural Information Processing Systems 36: Annual Conference on Neural*  
 692 *Information Processing Systems 2023, NeurIPS 2023, New Orleans, LA, USA, December 10 -*  
 693 *16, 2023*, 2023. URL [http://papers.nips.cc/paper\\_files/paper/2023/hash/33646ef0ed554145eab65f6250fab0c9-Abstract-Conference.html](http://papers.nips.cc/paper_files/paper/2023/hash/33646ef0ed554145eab65f6250fab0c9-Abstract-Conference.html).

694

695 Tianchen Zhao, Tongcheng Fang, Haofeng Huang, Rui Wan, Widayadewi Soedarmadji, Enshu Liu,  
 696 Shiya Li, Zinan Lin, Guohao Dai, Shengen Yan, Huazhong Yang, Xuefei Ning, and Yu Wang.  
 697 Vudit-q: Efficient and accurate quantization of diffusion transformers for image and video gen-  
 698 eration. In *The Thirteenth International Conference on Learning Representations*, 2025. URL  
 699 <https://openreview.net/forum?id=E1N1oxd63b>.

700

701

702 **A PROOFS**  
 703

704 **A.1 PROOF FOR THEOREM 1**  
 705

706 We prove the result reported in Theorem 1 in three steps. First, we demonstrate that the quantization  
 707 error for an orthogonal sequence transformation is the same as the quantization error on the sequence  
 708 transformed inputs:

709 
$$\mathcal{L}(\mathbf{X}; \mathbf{L}) = \mathcal{L}(\mathbf{LX}) \quad (10)$$
  
 710

711 *Proof.* This simply follows from the invariance of the Frobenius norm to orthogonal transforma-  
 712 tions.

713 
$$\begin{aligned} \mathcal{L}(\mathbf{X}; \mathbf{L}) &= \|\mathbf{L}^{-1}\mathcal{Q}(\mathbf{LX}) - \mathbf{X}\|_2^2 \\ 714 &= \|\mathbf{L}^{-1}\mathcal{Q}(\mathbf{LX}) - \mathbf{L}^{-1}\mathbf{LX}\|_2^2 \\ 715 &= \|\mathbf{L}^{-1}(\mathcal{Q}(\mathbf{LX}) - \mathbf{LX})\|_2^2 \\ 716 &= \|\mathcal{Q}(\mathbf{LX}) - \mathbf{LX}\|_2^2 \\ 717 &= \mathcal{L}(\mathbf{LX}) \end{aligned}$$

□

722 Secondly, for completeness, we prove the upper-bound reported in Equation 3. For quantization  
 723 scheme with minmax scales shared across all feature channels  $s_{ij} = \bar{s}_i$ :

724 
$$\mathcal{L}(\mathbf{x}_i) \leq \frac{d}{4} \frac{\mathbb{E} [\text{range}(\mathbf{x}_i)^2]}{(2^{b_i} - 1)^2} \quad (11)$$
  
 725  
 726  
 727

728 *Proof.*  
 729

730 
$$\begin{aligned} \mathcal{L}(\mathbf{x}_i) &= \mathbb{E} [\|\mathcal{Q}(\mathbf{x}_i) - \mathbf{x}_i\|_2^2] \\ 731 &= \mathbb{E} \left[ \left\| \mathbf{Q}^{-1} \left( \left[ \frac{\mathbf{x}_i}{\bar{s}_i} \right] + \mathbf{z}_i \right) - \mathbf{x}_i \right\|_2^2 \right] \\ 732 &= \mathbb{E} \left[ \left\| \left( \left[ \frac{\mathbf{x}_i}{\bar{s}_i} \right] + \mathbf{z}_i - \mathbf{z}_i \right) \bar{s}_i - \mathbf{x}_i \right\|_2^2 \right] \\ 733 &= \mathbb{E} \left[ \left\| \left( \left[ \frac{\mathbf{x}_i}{\bar{s}_i} \right] - \frac{\mathbf{x}_i}{\bar{s}_i} \right) \bar{s}_i \right\|_2^2 \right] \\ 734 &= \mathbb{E} \left[ \left\| \left( \left[ \frac{\mathbf{x}_i}{\bar{s}_i} \right] - \frac{\mathbf{x}_i}{\bar{s}_i} \right) \right\|_2^2 \bar{s}_i^2 \right] \\ 735 &\leq \mathbb{E} \left[ \left\| \frac{\mathbf{1}}{2} \right\|_2^2 \bar{s}_i^2 \right] \\ 736 &= \frac{d}{4} \frac{\mathbb{E} [\text{range}(\mathbf{x}_i)^2]}{(2^{b_i} - 1)^2}. \end{aligned}$$

□

750 Lastly, we bound the range using the norm 2:  
 751

752 
$$\text{range}(\mathbf{x}_i)^2 \leq 2 \|\mathbf{x}_i\|_2^2. \quad (12)$$
  
 753

754 Equality is attained whenever  $\hat{\mathbf{x}}_i$  consists of two non-zero entries  $-v$  and  $v$ , for which  $\text{range}(\mathbf{x}) =$   
 755  $2v$  and  $\|\mathbf{x}\|_2 = \sqrt{2}v$ .

756 Using this three steps we can write the proof for Theorem 1

756 *Proof.*

$$\begin{aligned}
 758 \quad \mathcal{L}(\mathbf{X}; \mathbf{L}) &\stackrel{10}{=} \mathcal{L}(\mathbf{LX}) \\
 759 \quad &= \sum_{i=1}^s \mathcal{L}(\mathbf{l}_i \mathbf{X}) \\
 760 \quad &\stackrel{11}{\leq} \frac{d}{4} \sum_{i=1}^s \frac{\mathbb{E} [\text{range}(\mathbf{l}_i \mathbf{X})^2]}{(2^{b_i} - 1)^2} \\
 761 \quad &\stackrel{12}{\leq} \frac{d}{2} \sum_{i=1}^s \frac{\mathbb{E} [\|\mathbf{l}_i \mathbf{X}\|_2^2]}{(2^{b_i} - 1)^2}
 \end{aligned}$$

762  $\square$

## 770 A.2 OPTIMAL BIT WIDTH ALLOCATION

772 We determine the optimal bit width allocation  $\mathbf{b}^*$  for an energy vector  $\mathbf{e}$  by determining the bit width  
 773 for which the ratio  $e_i/2^{2b_i^*} \approx e_i/(2^{b_i} - 1)^2$  is constant for all tokens:

$$\begin{cases} \frac{e_i}{2^{2b_i^*}} = k \\ \sum_{i=1}^s b_i^* = B \end{cases} \quad (13)$$

$$\Rightarrow b_i^* = \frac{\log_2 e_i - \log_2 k}{2} \quad (14)$$

$$\Rightarrow \sum_{i=1}^s \frac{\log_2 e_i - \log_2 k}{2} = B \quad (15)$$

$$\Rightarrow \log_2 k = \frac{1}{s} \sum_{i=1}^s \log_2 e_i - \frac{2B}{s} \quad (16)$$

$$\Rightarrow b_i^* = \frac{\log_2 e_i - \frac{1}{s} \sum_{i=1}^s \log_2 e_i + \frac{2B}{s}}{2} \quad (17)$$

$$\Rightarrow b_i^* = \log_2 \sqrt{e_i} + \underbrace{\frac{B - \sum_{i=1}^s \log_2 \sqrt{e_i}}{s}}_C \quad (18)$$

## 791 A.3 EFFECTIVENESS OF ENERGY CONCENTRATION

793 We demonstrate the effectiveness of the proposed Sequence Transform and Mixed precision scheme  
 794 by considering the upper bound in Equation 8 in two different settings. In order to simplify computa-  
 795 tion, we will consider  $\frac{e_i}{2^{2b_i}}$  instead of  $\frac{e_i}{(2^{b_i} - 1)^2}$  since the difference between the two quantities is  
 796 negligible for practical values of  $b_i$ .

### 798 1. Uniform Energy:

799 In this scenario we have  $e_i = E/s$  and  $b_i = B/s$ . We note that the energy for each token  
 800 is equal to the average of the squared eigenvalues  $\lambda_i^2$  of  $\mathbf{S}$ :

$$e_i = E/s = \text{Trace}(\mathbf{S})/s = \frac{1}{s} \sum_{i=1}^s \lambda_i^2 \stackrel{\text{def}}{=} \bar{\lambda}^2. \quad (19)$$

804 Therefore:

$$\frac{d}{2} \sum_{i=1}^s \frac{e_i}{2^{2b_i}} = \frac{d}{2} \sum_{i=1}^s \frac{\bar{\lambda}^2}{2^{2B/s}} = \frac{ds}{2} 2^{\log_2 \bar{\lambda}^2 - 2B/s} \quad (20)$$

### 809 2. Maximum Energy Concentration:

810 We consider a scenario in which the energy corresponds with the squared eigenvalues  $e_i =$

810  $\lambda_i^2$ . The optimal bit allocation is given by Equation 18:

$$b_i^* = \log \lambda_i + \frac{B}{s} - \underbrace{\frac{\sum_{i=1}^s \log_2 \lambda_i}{s}}_{\log_2 \bar{\lambda}} \quad (21)$$

Therefore:

$$\frac{d}{2} \sum_{i=1}^s \frac{e_i}{2^{2b_i}} = \frac{d}{2} \sum_{i=1}^s \frac{\lambda_i^2}{2^{\log \lambda_i^2 + \frac{2B}{s} - 2\log_2 \lambda}} = \frac{ds}{2} 2^{\log_2 \lambda^2 - 2B/s} \quad (22)$$

Comparing the two results is equivalent to comparing  $\log_2 \bar{\lambda}^2$  (uniform) and  $\bar{\log}_2 \lambda^2$  (max concentration). Using Jensen's inequality and the convexity of  $\log_2$ , we have:

$$\overline{\log_2 \lambda^2} = \mathbb{E}[\log_2 \lambda_i^2] \leq \log \mathbb{E}[\lambda_i^2] = \log_2 \overline{\lambda_i^2}. \quad (23)$$

Therefore, the Maximum Energy concentration strategies achieves a lower value than the uniform scheme.

864 **B EXPERIMENTAL DETAILS**  
865866 **B.1 LVMs**  
867868 **Baselines** We implement SmoothQuant, QuaRot, ViDiT-Q and SVDQuant closely following the  
869 details reported in the paper and the respective codebases. Specifically, for ViDiT-Q (Zhao et al.,  
870 2025) we use  $\alpha = 0.01$ , as reported in their PixArt- $\Sigma$  setup. For SVDQuant and SmoothQuant we  
871 use a default value of  $\alpha = 0.5$ .  
872873 **Quantization** In order to promote a fair comparison with the other models, for the results reported  
874 in Table 1, instead of using the 8-bits weight quatization scheme described in ViDiT-Q (8 bits for the  
875 FFN blocks, first and last transformer blocks), we use per-block weight and activation quantization,  
876 as described in SVDQuant (Li et al., 2025), which improves the ViDiT-Q results. In line with the  
877 SVDQuant methodology, we retain the depth-wise convolutions within the feed-forward layers of  
878 the SANA transformer blocks in full precision. Meanwhile, the two point-wise convolutions are  
879 quantized by treating them as linear layers. Notably, unlike the original SVDQuant implementation,  
880 our experiments do not incorporate GPTQ at any stage. The activation-quantization only results  
881 reported in Figure 4b and Figure 7 use 4 bits per token quantization.  
882883 **STaMP** For the STaMP results, excluding the specific ablation study, we use 64 high-precision  
884 tokens, which results in an effective activation bit-width of 4.0625 bits on the PixArt- $\Sigma$  model and  
885 4.125 bits on the SANA model. Non-STaMP result do not use any mixed precision tokens.  
886887 **B.2 LLMs**888 **Quantization** We use dynamic quantization for the KV cache and activations. Quantization scales  
889 and offsets are determined per token, sequence, and (for KV) head. We follow (Ashkboos et al.,  
890 2024; Sun et al., 2025) and only quantize weights, KV cache, and inputs to linear layers within  
891 the transformer block. We use round-to-nearest weight quantization, as weights are unaffected by  
892 STaMP—more advanced weight quantization schemes could improve results further, but this is per-  
893 perpendicular to our contribution. we range set the weights by computing the weight quantization  
894 squared error for a grid of candidate ranges and selecting the candidate with lowest error. For fair-  
895 ness, for all experiments (incl. baselines) we keep the first 64 tokens in 8 bits, which gives an  
896 effective bit width of 4.125 for both STaMP and non-STaMP results.  
897898 **Baselines** For SmoothQuant, we calibrate the scales based on the Wikitext-2 training dataset acti-  
899 vations. For QuaRot, we follow the original paper and reduce the minmax activation range by 10%.  
900 For FlatQuant, we use their recommended settings for all models (e.g. training for 15 epochs on 128  
901 Wikitext-2 training sequences).  
902903 **STaMP** The first token in most LLMs acts as an attention sink Xiao et al. (2024); Gu et al. (2025),  
904 and typically contains massive outliers Sun et al. (2024). Keeping the first token in 8 bits helps to  
905 accurately represent these massive outliers. To ensure the massive outlier stays in the first token,  
906 STaMP is not applied to the first token. Note that the baselines that do not use STaMP’s transform,  
907 do benefit from keeping the first token (and next 63) in high-precision in our experiments.  
908909 **B.3 NOTES ON THE RUNTIME ESTIMATION**  
910911 **B.3.1 DWT OVERHEAD**  
912913 To compute the overhead associated with the sequence and feature transforms, we measured the  
914 time required to run a single denoising step with the original PixArt- $\Sigma$  model, and compared it with  
915 the modified architectures (having the extra transform operations). Measurements are performed on  
916 an A100-SXM4-80GB GPU using python 3.10.12, PyTorch 2.5.1+cu121, and CUDA drivers 12.5.  
917 Hadamard transforms are based on the CUDA-accelerated kernels from the fast-hadamard-transform  
918 package <sup>3</sup>. For Haar DWT operations, we built a specialized CUDA kernel, optimized for applying  
919920 <sup>3</sup><https://github.com/Dao-AI-Lab/fast-hadamard-transform>

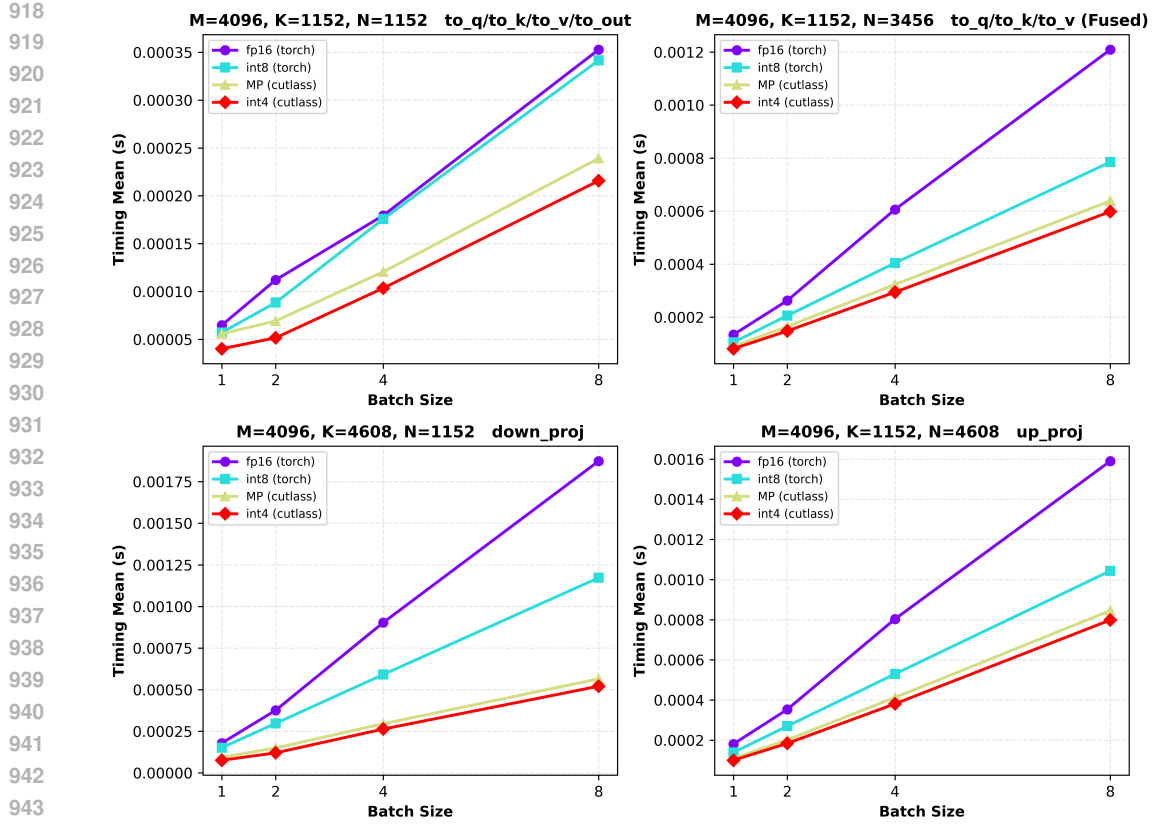


Figure 8: Visualization of runtime estimation in terms of latency on CUDA for running matrix multiplication kernels with different data types, shapes, and batch sizes, averaged over 1000 runs. The proposed mixed precision approach has a minimal overhead that does not depend on the batch size.

DWT over the sequence dimension. The increased latency measured with the Hadamard applied on the sequence dimension can be mainly attributed to the memory reshaping operations required to use the fast-hadamard-transform kernel.

### B.3.2 MIXED-PRECISION MATRIX MULTIPLICATION

When using STaMP, the first tokens of the activation tensors are stored at a higher bit width with respect to the subsequent ones (8 and 4 bits in our experimental settings). This implies that the subsequent linear operation should perform part of the computation with higher precision. The number of extra bit operations for the 8 bit part is minimal (about 1.56% on PixArt-Sigma).

It is important to note that STaMP 4-8 bits mixed precision scheme drastically reduces the number of binary operations when compared to *int8* matrix multiplications. However, the latency measurements are heavily influenced by the support for specific data types and operations in the hardware and software stack of the target device. Demonstrating the effectiveness of *int4* quantization is an important step towards developing support for more power-efficient solutions in commercial-grade hardware.

We assessed the effectiveness of the proposed mixed precision design by measuring the time to perform a mixed precision matrix multiplication on CUDA, and we compared to performing the same operation with *fp16*, *int8* or *int4* data types. When using Nvidia hardware, one can take advantage of Tensor Cores to accelerate low-precision operations and allow higher computational throughput. PyTorch uses Tensor Cores kernels for most of the low-precision data types (such as *tf32*, *fp16*, *bf16*, *int8*), but the PyTorch stack lacks an *int4* accelerated kernel. Following the

972 procedure from Sun et al. (2025)<sup>4</sup>, we used a Cutlass-based *gemm* kernel with minor modifications  
 973 to the python bindings to enable inplace operations.  
 974

975 In Figure 8, we report the outcome of our benchmarks for different batch sizes and for the tensor  
 976 shapes used in the Pixart- $\Sigma$  architecture. The measured overhead for the mixed-precision matrix  
 977 multiplication over the *int4* one for batch-size 2 (required for generating a single output image) vary  
 978 from about 30% (for smaller shapes) to approximately 10% (for fused Q/K/V computation and up  
 979 projection). Increasing the batch size to 8 reduces the relative overhead to under 10% on all layers.  
 980

981 One should consider that our Mixed-Precision implementation essentially runs two matmuls: one  
 982 using the custom cutlass kernel over the *int4* data double-packed into an *int8* tensor, the other using  
 983 the standard torch *int8* kernel over the first 64 tokens and writing the results on the first 64 tokens  
 984 of the output tensor. For batch size 2, we also perform an additional *int8* operation over the first  
 985 64 tokens of the second sample. For batch sizes 4 and larger we slice the tensors to retrieve the  
 986 first 64 tokens of each batch element and pack into contiguous memory before running a single  
 987 *int8* matmul. Additional memory transfer optimization and kernel fusion could further decrease the  
 988 overhead introduced by the STaMP operations.  
 989

## 990 C ADDITIONAL RESULTS

### 991 C.1 LVMS

992 We report additional results for the setups described in Section 5, including an ablation of the effect  
 993 of STaMP on different activations (Table 4), bit width vs SQNR comparison against per-block acti-  
 994 vation quantization (Figure 10), and additional metrics (Table 5) and visualizations (Figure 11) for  
 995 the results reported in the main text.  
 996

### 997 C.2 LLMS

998 We report additional LLM evaluation involving common few-shots reasoning tasks in Table 6. The  
 999 evaluation is performed using the *lm-eval-harness* toolkit (Gao et al., 2024).  
 1000

## 1001 D USE OF LLMS

1002 Large Language Models have been used only for sentence rephrasing and grammar check, which  
 1003 resulted in minor alterations to the paper text.  
 1004

1005  
 1006  
 1007  
 1008  
 1009  
 1010  
 1011  
 1012  
 1013  
 1014  
 1015  
 1016  
 1017  
 1018  
 1019  
 1020  
 1021  
 1022  
 1023  
 1024  
 1025  
<sup>4</sup><https://github.com/ruikangliu/FlatQuant>

1026 Table 4: Effect of A4 activation quantization on single activations of the Pixart- $\Sigma$  model on the  
 1027 Image SQNR. Each entry corresponds to a model for which only the corresponding input activation  
 1028 is quantized. Note that STaMP has little to no effect on *attn2.to\_out* since the structure is determined  
 1029 by pooled textual embedding, which does not present the same correlation structure as the other  
 1030 activations in the network.  
 1031

Transform	<i>attn1</i>	<i>attn1.to_out</i>	<i>attn2.to_q</i>	<i>attn2.to_out</i>	<i>ffn.up_proj</i>	<i>ffn.down_proj</i>
Identity	6.01	10.09	0.40	15.48	1.15	4.92
QuaRot	13.80	16.01	16.29	23.20	11.36	8.42
STaMP	7.68	13.89	11.60	15.49	8.75	9.61
QuaRot+STaMP	15.28	16.78	18.31	23.23	13.84	14.91

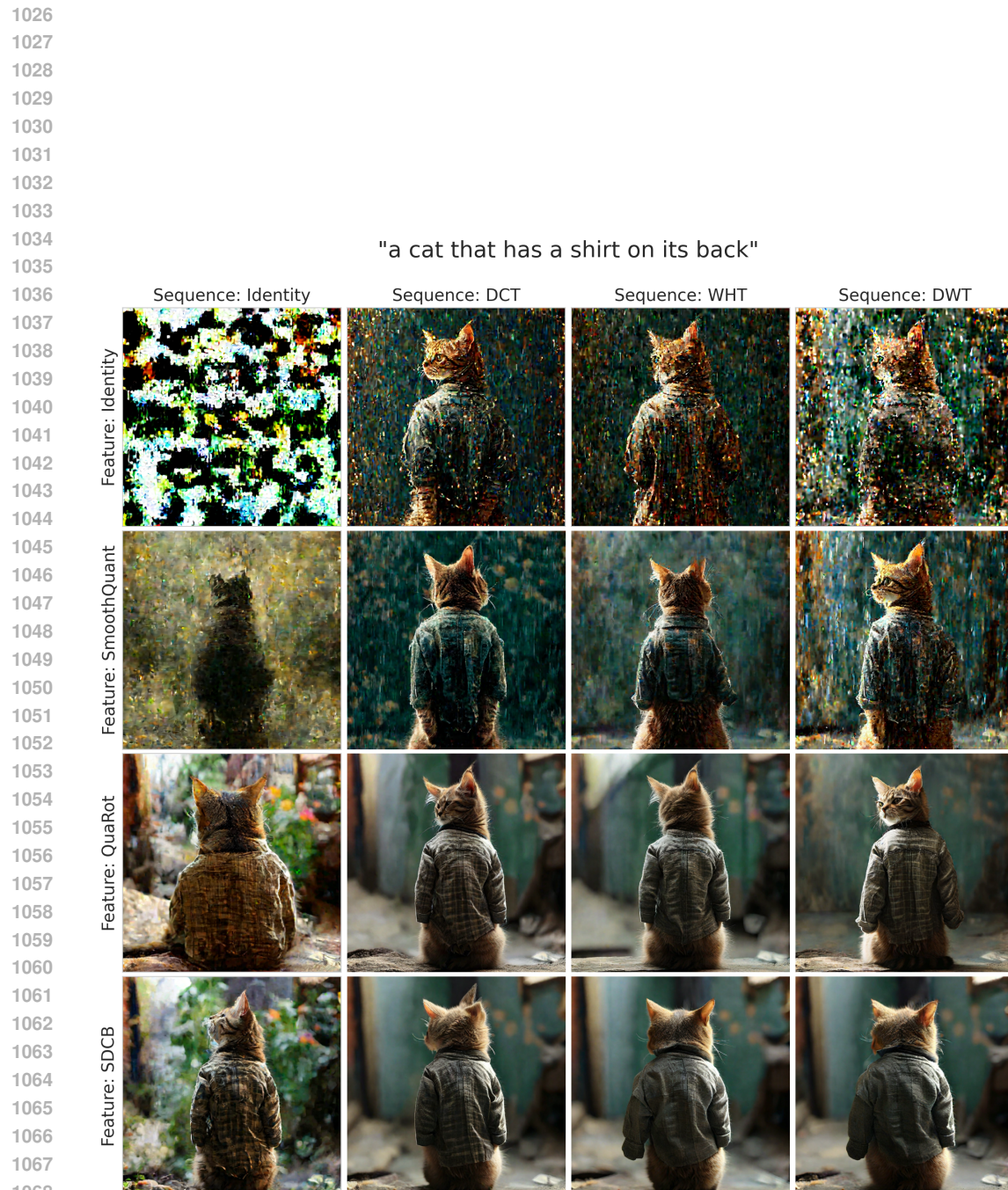


Figure 9: Visualization of the Images generated with A4 activation quantization and several combination of Feature and Sequence transforms for the Pixart- $\Sigma$  architecture. The images refer to the same setup described in Figure 7.



Figure 10: Tradeoff between SQNR and bit width for per-token activation quantization (pt) per-block activation quantization (pb) at different block size (from 16 to 1024), and per-token with STaMP (pb+STaMP) at varying number of high precision tokens on the PixArt- $\Sigma$  model. We consider 16 bits scales for each scale parameter. The visualization correspond to the Prompt 'A guy with a backpack looking at the ground to his left.'

1134  
 1135  
 1136  
 1137  
 1138  
 1139  
 1140  
 1141  
 1142  
 1143  
 1144  
 1145  
 1146  
 1147  
 1148  
 1149  
 1150  
 1151  
 1152 FP32  
 1153 RTN  
 1154 ViDiT-Q  
 1155 SVDQuant  
 1156  
 1157  
 1158  
 1159  
 1160 RTN +STaMP  
 1161 ViDiT-Q +STaMP  
 1162 SVDQuant +STaMP  
 1163  
 1164 “*portrait of an army of wild*  
 1165 *mountain hares are roaming*  
 1166 *the streets of central*  
 1167 *Stockholm, summertime,*  
 1168 *warm and sunny, sunset life*  
 1169 *style stock image popular no*  
 1170 *text prompt trend. pinterest*  
 1171 *contest winner”*



Figure 11: Visualization of a sample generation for the SANA for the results reported in Table 1.

1171  
 1172  
 1173  
 1174  
 1175  
 1176  
 1177  
 1178  
 1179  
 1180  
 1181  
 1182  
 1183  
 1184  
 1185  
 1186  
 1187

Table 5: Additional metrics for the experiments reported in Table 1.

Dataset	LVM	Method	STaMP	CLIP	CLIP IQA	SQNR (latent)
COCO	PixArt- $\Sigma$	FP		31.54	0.91	$+\infty$
		RTN	✗	31.23	0.79	0.19
		SVDQuant	✓	31.88	0.91	0.49
		ViDiT-Q	✗	31.68	0.91	0.96
	SANA	SVDQuant	✓	31.76	0.91	1.47
		FP		31.63	0.87	0.73
		RTN	✗	31.92	0.87	1.03
		ViDiT-Q	✓	31.85	0.89	$+\infty$
MJHQ	PixArt- $\Sigma$	FP		31.85	0.89	3.39
		RTN	✗	31.94	0.89	4.09
		SVDQuant	✓	31.83	0.90	4.61
		ViDiT-Q	✗	31.88	0.90	5.30
	SANA	FP		31.79	0.89	4.63
		RTN	✗	31.82	0.89	5.42
		SVDQuant	✓	31.46	0.85	$+\infty$
		ViDiT-Q	✗	29.90	0.75	0.28
	SANA	FP		30.96	0.87	0.71
		RTN	✓	31.13	0.86	1.27
		SVDQuant	✓	31.28	0.87	1.86
		ViDiT-Q	✗	30.97	0.81	0.86
	PixArt- $\Sigma$	FP		31.20	0.83	1.31
		RTN	✓	31.57	0.83	$+\infty$
		SVDQuant	✗	31.51	0.84	4.45
		ViDiT-Q	✓	31.60	0.84	5.39
	PixArt- $\Sigma$	FP		31.52	0.83	5.69
		RTN	✓	31.55	0.83	6.46
		SVDQuant	✗	31.60	0.83	5.76
		ViDiT-Q	✓	31.60	0.83	6.65

1242  
 1243  
 1244  
 1245  
 1246  
 1247  
 1248  
 1249  
 Table 6: LLM evaluation on Common Reasoning tasks. The experimental setup is equivalent to the  
 1250 one described in Table 2.  
 1251

Task	STaMP →	Llama 3 8B		Llama 3.2 1B it		Llama 3.2 3B it		Qwen 2.5 3B it	
		✗	✓	✗	✓	✗	✓	✗	✓
	FP	54.4		36.1		46.4		56.0	
<i>arc challenge</i>	RTN	43.9	44.1	27.9	28.4	35.7	35.9	36.6	37.0
	SmoothQuant	40.3	40.2	30.5	30.5	34.5	34.6	39.2	39.3
	QuaRot	39.0	38.7	30.5	30.5	37.4	37.1	42.8	43.2
	FlatQuant	52.0	52.5	33.9	34.2	44.4	45.5	52.0	54.0
	FP	84.2		70.7		79.7		83.5	
<i>arc easy</i>	RTN	75.2	75.8	56.2	56.3	63.6	63.8	66.7	66.8
	SmoothQuant	71.4	72.1	61.7	62.4	64.5	65.1	69.0	69.3
	QuaRot	71.5	71.3	58.2	58.3	66.5	66.5	73.5	73.6
	FlatQuant	81.3	82.4	67.6	67.8	77.5	77.7	82.2	82.4
	FP	61.3		44.3		52.8		56.2	
<i>hellaswag</i>	RTN	39.2	50.2	31.0	34.0	37.2	41.9	32.4	33.2
	SmoothQuant	39.1	47.4	33.3	36.5	40.1	45.3	33.3	33.8
	QuaRot	49.5	51.2	37.9	38.9	45.9	46.9	34.0	33.9
	FlatQuant	58.7	59.7	41.2	41.9	50.4	50.8	53.6	54.5
	FP	71.1		55.1		63.3		59.3	
<i>lambada</i>	RTN	0.2	1.2	0.3	0.9	0.7	3.6	0.0	0.0
	SmoothQuant	0.5	2.7	0.6	1.6	2.4	9.0	0.0	0.0
	QuaRot	15.1	24.6	16.4	20.6	37.6	40.6	0.0	0.0
	FlatQuant	67.1	67.1	44.1	48.3	58.1	58.9	55.0	57.5
	FP	81.1		74.0		77.3		78.0	
<i>piqa</i>	RTN	75.4	76.5	66.2	66.5	69.7	70.3	71.5	71.6
	SmoothQuant	74.1	74.3	68.7	68.8	71.6	72.0	72.1	72.3
	QuaRot	74.2	73.9	68.9	68.4	70.9	70.7	73.1	72.9
	FlatQuant	79.4	80.2	72.1	73.0	76.1	75.7	77.5	77.6
	FP	77.5		62.0		70.6		70.6	
<i>winogrande</i>	RTN	71.0	71.0	55.2	55.2	63.1	63.1	62.0	62.0
	SmoothQuant	70.8	70.8	54.9	54.9	64.8	64.8	65.6	65.6
	QuaRot	70.8	70.8	57.6	57.6	62.6	62.6	65.9	65.9
	FlatQuant	75.2	74.9	58.6	60.1	66.4	68.8	66.6	68.1
	FP	69.7		55.7		63.8		65.5	
Average	RTN	50.8	53.1	39.4	40.2	45.0	46.5	44.9	45.1
	SmoothQuant	49.4	51.2	41.6	42.5	46.3	48.5	46.5	46.7
	QuaRot	53.3	55.1	44.9	45.7	53.5	54.1	48.2	48.2
	FlatQuant	67.4	67.9	50.9	52.3	60.7	61.5	62.7	63.9